Multifunctional Nanostructure of Au-Bi_2O_3 Fractals for CO_2 Reduction and Optical Sensing

Thanh Tran-Phu[†a], *Rahman Daiyan*[†b], *Zelio Fusco*[†a], *Zhipeng Ma,*[b] *Lina Raihana Abd Rahim*[a], *Alexander Kiy*[c], *Patrick Kluth*[c], *Xuyun Guo*[d], *Ye Zhu*[d], *Hongjun Chen*[a], *Rose Amal*[b], *Antonio Tricoli*[a]

[a] Nanotechnology Research Laboratory, College of Engineering and Computer Science, The Australian National University, Canberra, ACT 2601, Australia
[b] Particles and Catalysis Research Laboratory, School of Chemical Engineering, The University of New South Wales, Sydney, NSW 2052, Australia
[c] Department of Electronic Materials Engineering, Research School of Physics, Australian National University, Canberra, ACT 2601, Australia
[d] Department of Applied Physics, the Hong Kong Polytechnic University, Hung Hom, Hong Kong, PR China.

[†] Authors contributed equally

Corresponding Authors
*Email: antonio.tricoli@anu.edu.au
r.amal@unsw.edu.au

Abstract

The development of nanomaterials with multifunctional properties presents a viable business case for potential scale-up of nanomaterial fabrication. Hence, the design and engineering of structures as well as tuning of active sites are crucial in generating multifunctional properties in nanomaterials. In this regard, we demonstrate a three-dimensional (3D) fractal structure of Au-Bi_2O_3 with fractal dimension (D_f) of ≈ 1.80, which is obtained from the small-angle X-ray scattering (SAXS) measurement and through the box counting algorithm. The fractal structures, fabricated via a one-step direct synthesis, gives a homogeneous distribution of catalytically active nanocrystals Au and Bi_2O_3 on a 3D platform with high active surface area, resulting in a strong enhancement of its localized electric field. Therefore, when applied as a catalyst for electrochemical CO_2 reduction reactions (CO_2RR) and optical gas sensing, the material displays an excellent performance. Specifically, the fractal structure exhibits a high selectivity towards the formation of formate, achieving a very high Faradaic efficiency of 97% and high mass-specific formate current density of -54 mA mg^{-1} at -1.1 V vs reversible hydrogen electrode (RHE). Similarly, this structure displayed a plasmonic shift as high as ~ 5 nm for 4 vol% acetone sensing with a detection limit of 100 ppm towards different volatile organic compounds (VOCs).

Keywords: Multifunctional, Fractals, Gold Bismuth Oxide, SAXS, CO_2 Reduction, Optical Gas Sensing

Introduction

Inspired by multifunctional structural material systems in nature like human skin or bird feathers, the development of nanomaterials with incorporated multiple functionalities is an emerging field with a great potential for practical applications.[1-4] For instance, carbon nanotube bristles have been developed for a range of applications: narrow space cleaning, chemical adsorption, and electrical contact.[5] Similarly, metalenses with multifunctional photonic components can be applied to different areas including wearable display and bio-imaging.[6] SnO_2-CNT nanohybrids were reported for adsorbent, catalyst, and antimicrobial agent.[7] Very recently, bimetallic Sn-Bi alloy was employed for carbon dioxide reduction reaction (CO_2RR) and water purification.[8] Often, the functionality in nanomaterials is intrinsically bounded to the structure, and many multipurpose devices have been shown to have complex recursive features across different length scales.[9, 10] Indeed, complex and disordered materials are rapidly proving their functions in different fields like catalysis,[11, 12] photonics,[13-15] or sensing.[16, 17]

In this panorama, fractal structures are appealing candidates to tame the complexity toward tailorable multifunctional devices thanks to their endowment of showing iterative and stochastic organization. Driven by recursion, fractals are objects that possess self-similar properties replicating over finite range of magnitudes. These patterns are also very common in the natural world as many of *natural laws* follow a fractal scaling rule.[18] Hence, understanding the design principle of these structures is of paramount importance to design man-made structural materials for practical applications. In fact, fractals have found widespread applications –amongst many– in the telecommunication sector,[19] electronics,[20] optics,[21] chemistry,[22] and biology.[23] Particularly, the fractal structure of the alkylketene dimer (AKD) shows excellent water-repellent property[24], or the enhancement of light trapping has been shown in the random fractal of silicon nanowires.[25] Recently, disordered aggregates of metal oxides have shown advantages for water splitting[12] and CO_2RR.[26] In light of this extraordinary potential of fractals, it remains to be seen if such structures can be engineered for multifunctional applications such as clean energy harvesting, sensing, medicine, and environmental remediation.

In this work, we designed and fabricated a multifunctional platform based on the three-dimensional (3D) distribution of Au nanocrystals onto tailored fractals of Bi_2O_3. We take advantage of the stochastic Brownian motion in supersaturated aerosol to drive the self-assembly of Au and Bi_2O_3 nanocrystals simultaneously to form a novel hybrid 3D metal-semiconductor media. [27, 28] The structure consists of Au nanoparticles, with tunable long-range uniformity and density, dispersed in fractal scaffolds of Bi_2O_3. Generally, a nonconductive binder is used in a conventional process of fabricating films such as the drop-casting.[29, 30] However, with the advantage of the direct fabrication of the fractal structure on substrates via the hot-aerosol synthesis, a binder-free film, which facilitates the electron transport and enhances the chemically active surface area and density of the electrocatalyst material,[31] is formed in a facile manner. The fractality of Au-Bi_2O_3 was then measured by means of synchrotron-based small-angle X-Ray scattering (SAXS) and was found to be in agreement with the image analysis. This structure was tested for electrochemical carbon dioxide reduction reactions (CO_2RR), and it demonstrated exceptional selectivity towards formate (97% with a high mass specific formate partial current density of -54 mA mg^{-1} at -1.1 V vs RHE). Additionally, the inclusion of plasmonic Au nanoparticles within Bi_2O_3 has also been exploited to build a fully operational optical sensor based on localized surface plasmonic resonance (LSPR). As a result, the fractal Au-Bi_2O_3 demonstrates excellent sensing properties towards gaseous volatile organic compounds (VOCs) with lower detection limits of 100 ppm at room temperature. The multifunctionality of the Au-Bi_2O_3 fractals was investigated experimentally and theoretically, and a mechanism model for the superior performance is proposed. The admirable efficiencies obtained toward gas sensing and CO_2RR can be ascribed to the synergistic coupling of (i) the highly porous fractal platform, which presents numerous active sites for CO_2 and VOCs adsorption, and (ii) the enrichment of the electron density originating from the enhancement of the localized electric field due to the presence of gold nanoparticles distributed homogeneously throughout the 3D fractal film.

Results and Discussion

Figure 1a shows a schematic rendering of the Au-Bi_2O_3 fractal by a hot-aerosol approach. In this process, liquid bismuth and gold precursors were separately dissolved in combustible solvents before being injected into a double-flame spray pyrolysis (DFSP) system (**Methods**). DFSP has been reported previously to fabricate nanomaterials for a variety of applications such as electrocatalysis, photocatalysis, and gas sensing. [27, 28, 32, 33] Typically, the precursors were atomized by an oxygen dispersion flow to form micro-droplets of liquid precursor before being ignited by a surrounding pilot flame. The evaporation of solvents and the decomposition of the metallic precursors by the high temperature of the flame lead to an oversaturated aerosol of the target metal/metal oxide, which nucleates and grows by means of Brownian coagulation and/or coalescence. Finally, the incoming nanoparticle aerosol self-assembles in a fractal structure of homogeneously dispersed Au and Bi_2O_3 on selected substrates, including (i) carbon fiber paper (CFP) and (ii) glass substrates by means of diffusion-limited cluster-cluster aggregation. [34, 35] Low magnification SEM images of the Au-Bi_2O_3 fractals on the CFPs (inset **Figure 1b**) and on the glass substrates (inset **Figure 1c**) indicate a large-scale uniformity of the catalytic layers. Moreover, investigation of the catalytic layer at higher magnification (**Figure 1b,c**) reveals an ultraporous nanoparticle network with a fractal structure, which is similar to previous reports on pure TiO_2[16], ZnO[36], and Eu-doped Y_2O_3.[37]

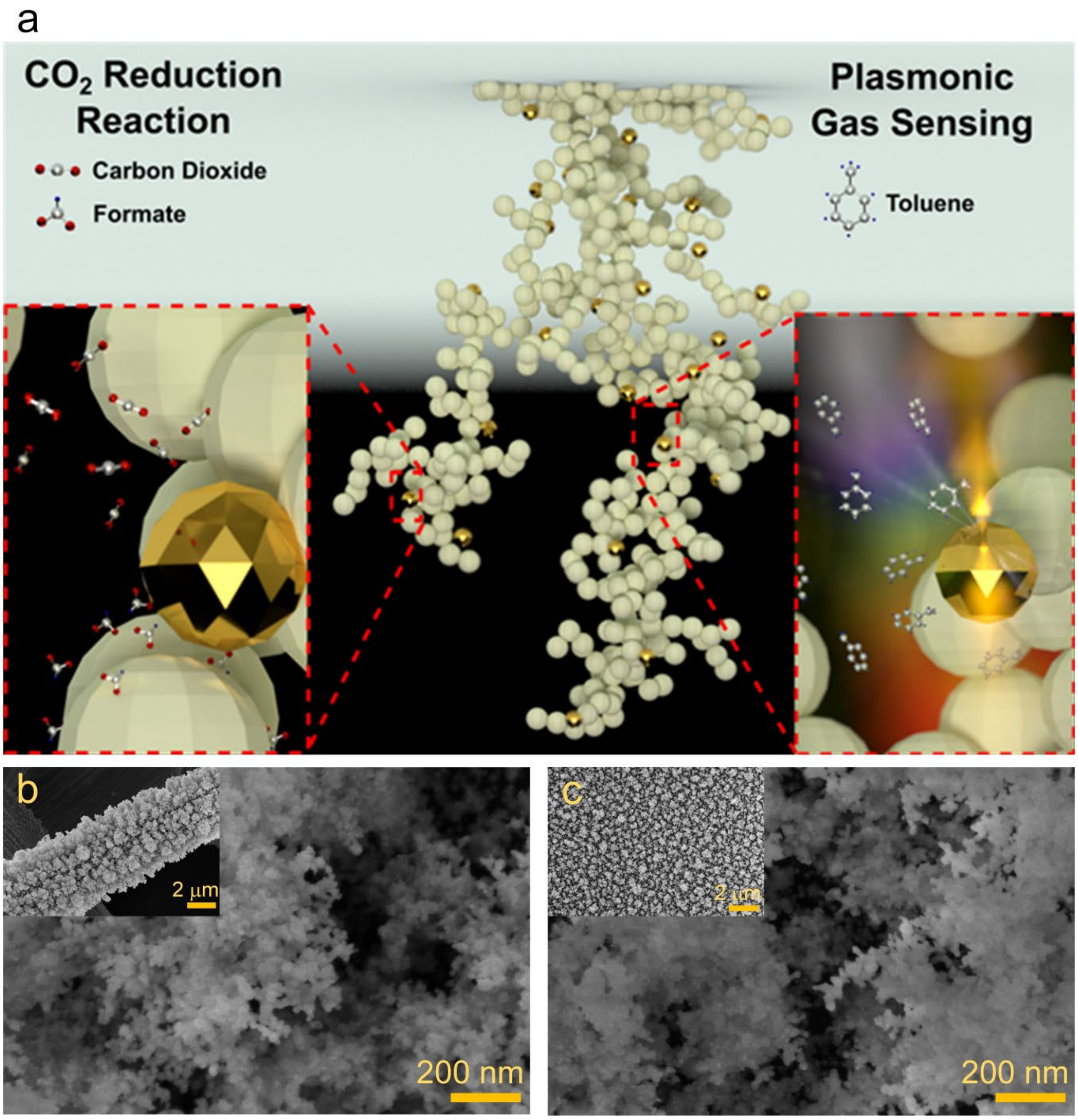

Figure 1. (a) Schematic diagram of the Au-Bi_2O_3 fractal with the enlarged regions representing CO_2RR to formate (on the left) and optical gas sensing to toluene (on the right). (b, c) SEM images at different magnifications of the sample on (b) carbon fiber paper (CFP) and (c) glass substrate.

After establishing the morphology, we attained the fractal dimension, D_f, of the Au-Bi_2O_3 clusters using the box counting method implemented in Fraclac, an ImageJ plugin[16, 38] and compared with the small-angle X-ray scattering (SAXS).[39-41] Generally, particle aggregates which are obtained by the aerosol synthesis exhibit a D_f ranging from 1.6 to 2.5.[42-44] The results of the box counting analysis are shown in **Figure 2a-c**. Top-view SEM images of the Au-Bi_2O_3 films were used for this analysis (**Figure 2a**). The generated image from the analysis is presented in the inset of **Figure 2a**. The theoretically calculated slope of the double-log plot (shown in **Figure 2b**) indicates the fractal dimension of the film, which is 1.79. The lacunarity, Λ, of the film, which indicates the heterogeneity of the structure was also evaluated. As shown in **Figure 2c**, the maximum of the lacunarity is between 150 and

200 nm. As a 2D projection image of the object was used in the box counting analysis, the upper limit of D_f to be determined is 2.0.[45] Therefore, the small-angle X-ray scattering (SAXS) measurement of the Au-Bi_2O_3 films was independently pursued to determine the fractal dimension of the samples in 3D space.

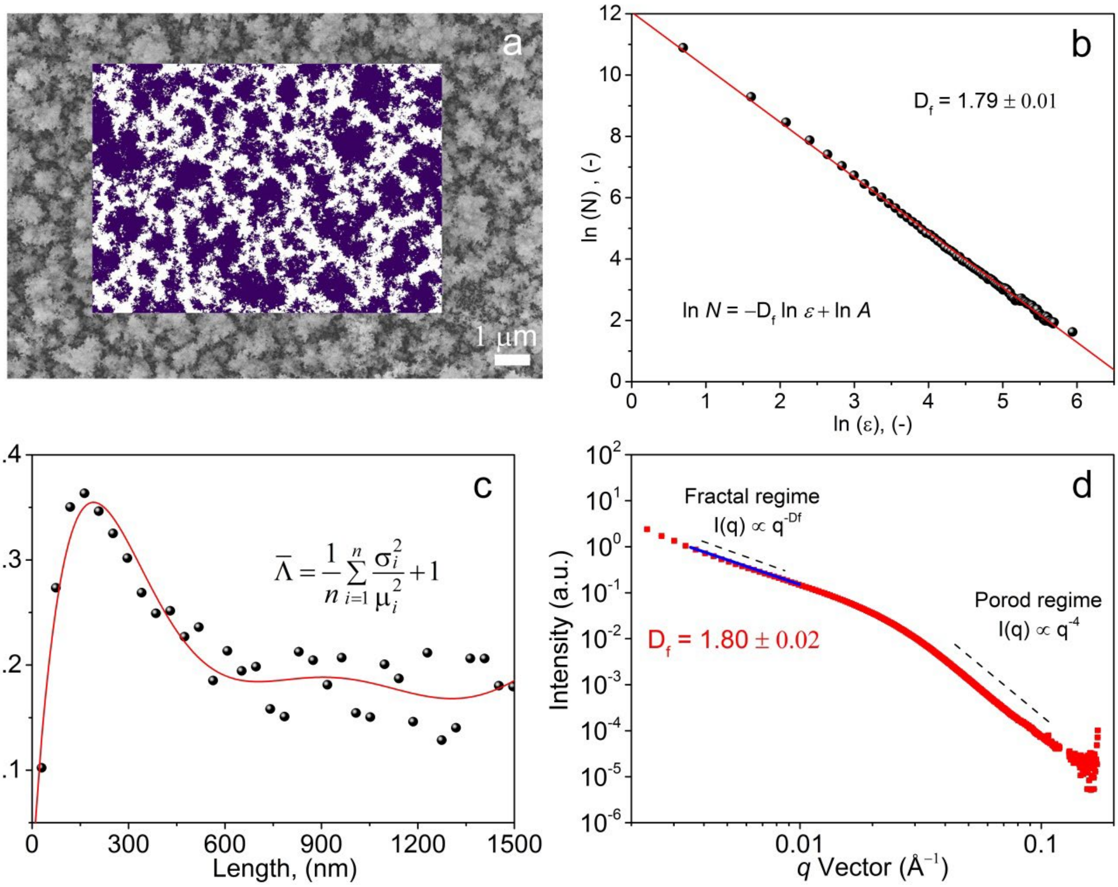

Figure 2. Fractal analysis of the Au-Bi_2O_3. (a-c) Fractal analysis obtained from the box counting method with (a) SEM image of the Au-Bi_2O_3 (inset: a reduced size generated from the fractal analysis), (b) double-logarithmic plot of the lnε (ε, box size) and lnN (N, number of boxes), which shows the fractal dimension of 1.79 as the slope of the plot, and (c) lacunarity of the Au-Bi_2O_3 film. (d) Double-logarithmic plot of the scattering intensity and the scattering vector q measured by small angle X-ray scattering (SAXS) of the Au-Bi_2O_3 film on a glass substrate.

In principle, when matter is radiated by X-rays, it scatters the beam, and by measuring the intensities of the scattered radiation as a function of the scattering angle, information about the structure can be obtained.[45, 46] **Figure 2d** presents the scattering intensity of the film from SAXS measurement as a function of the scattering vector q, which is defined as $q = 4\pi/\lambda \sin(\theta/2)$, where λ is the wavelength and θ is the scattering angle. Typically, the scattering patterns obtained from SAXS present three regimes, (i) Porod, (ii) mass-fractal and (iii) Guinier regime. The Porod regime (high-q regime) is characterized by q^{-4} decay of the scattered intensity for the surface of the primary particle. At smaller q-values, the mass-fractal regime with $1 < D_f < 3$ is observed, and the Guinier regime at low-q presents the mass-fractal agglomerates of aggregates.[40, 41, 45] In the case of our Au-Bi_2O_3 fractals, the mass-fractal structure determination is of most interest, and the D_f of the Au-Bi_2O_3 film was measured to be 1.80. Our fractal analysis from SAXS is consistent with the counting box analysis, and this is in a good agreement with fractal dimension of structures fabricated from the hot-aerosol synthesis in literature.[41, 47] Notice that the fractal dimension of Au-Bi_2O_3 is lower than our previously reported fractal Bi_2O_3 using SFSP (1.85), implying that the current structure has more open structure, which are crucial to enhance the active surface for catalytic and gas sensing applications.[36, 48]

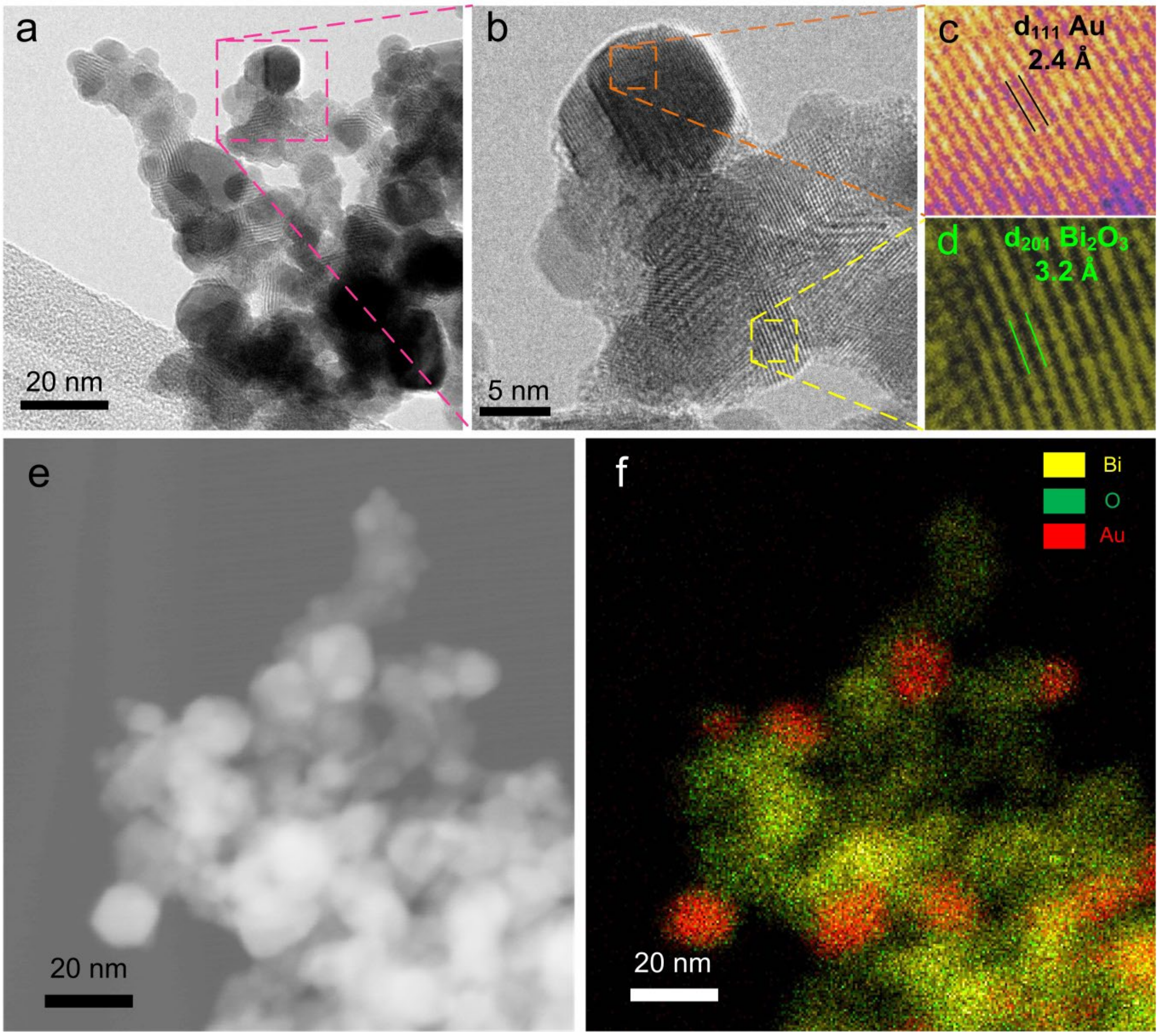

Figure 3. Structural characterizations of the Au-Bi_2O_3 fractal. (a-d) TEM images of the structure at different magnifications with the enlarged fringes of the (c) gold and (d) Bi_2O_3, (e) STEM image and (f) corresponding EDS mapping image of the overlay of the three elements with Bi (yellow), O (green), Au (red) respectively.

The crystallinity and composition of the Au-Bi_2O_3 fractal was then investigated by X-ray diffraction (XRD). **Figure S1** shows representative XRD patterns of Au-Bi_2O_3 fractals. Assignable peaks to the tetragonal (β-phase) Bi_2O_3 (JCPDF# 78-1793) with a (201) predominant plane and to the cubic structure of Au (PDF# 99-0056) with a (111) predominant plane are observed. It is interesting to note that the DFSP system is capable of generating the most active phase (β-phase) of Bi_2O_3,[49] amongst the six polymorphic forms, for catalytic applications. The morphological structure and local composition of the Au-Bi_2O_3 fractal were further analyzed by transmission electron microscopy (TEM) and energy dispersive spectroscopy (EDS). **Figure 3a-d** shows TEM images of highly crystalline Au-Bi_2O_3 fractals. An average grain size of ~ 12 and 14 nm can be observed (**Figure S2**) for Au and Bi_2O_3, respectively. High-resolution TEM reveals lattice fringes corresponding to the (111) plane of Au (**Figure 3c**) and the (201) plane of Bi_2O_3 (**Figure 3d**), in agreement with the XRD spectra. The elemental mapping of the Au-Bi_2O_3 (**Figure 3e-f)** shows a homogeneous dispersion of the Au and Bi_2O_3 components throughout the fractal structure. The surface chemical composition of the Au-Bi_2O_3 fractals (**Figure S3)** was probed by X-ray photoelectron spectroscopy (XPS). High resolution XPS spectra of the Bi 4f (**Figure S3b**) and Au 4f (**Figure S3c**) core levels indicates the formation of Bi_2O_3 and metallic Au. The double peaks at the binding energy of 164.66 and 159.35 eV for the Bi correspond to the Bi $4f_{5/2}$ and Bi $4f_{7/2}$ in an oxide bond. The double component at the binding energy of 87.87 and 84.20 eV confirms the formation Au $4f_{5/2}$ and Au $4f_{7/2}$ in metallic bond, in alignment with literature.[50, 51] We further carry out thermogravimetric analysis (TGA) measurement with our Au-Bi_2O_3 which reveal negligible carbon content within our catalyst (**Figure S4**). Overall, these characterizations provide strong evidence of the formation of well-dispersed Au-Bi_2O_3 composites organized in a fractal structure.

The electrochemical performance of the Au-Bi_2O_3 fractals for electrochemical reduction of CO_2 was investigated by potentiostatic experiments. The polarization curves (**Figure 4a**) carried out in a Ar and a CO_2 saturated 0.1 M $KHCO_3$ with Au-Bi_2O_3 indicate similar onset potential (-0.6 V) for carbon dioxide reduction reaction (CO_2RR) and the competing hydrogen evolution reaction (HER), although the maximum current density (*j*) attained in the CO_2 environment is much higher. Note at the range of -0.7 V to -0.85 V, the slightly higher current density of the Au-Bi_2O_3 in the Ar-saturated 0.1 M $KHCO_3$ environment may arise from the HER reaction.[52] At -1.1 V, the *j* attained in a CO_2 and Ar environments are -22.6 mA cm^{-2} and -4.8 mA cm^{-2}, respectively. Bulk CO_2 electrolysis was carried out with the Au-Bi_2O_3 fractals at different potentials and the product distribution is reported in **Figure 4b**. Notably, the Au-Bi_2O_3 fractals are highly selective towards the formation of $HCOO^-$, attaining a very high faradaic efficiency towards formate product (FE_{HCOO^-}) of 97% at -1.1 V, whereas both FE_{CO} and FE_{H2} are negligible. This selectivity is much more enhanced compared to the control Bi_2O_3 which can display a maximum FE_{HCOO^-} of ~87% at -1.2 V vs RHE (**Figure S5a**). Furthermore, the Au-Bi_2O_3 was demonstrated to be stable during CO_2RR, as indicated by the representative chronoamperometry (*i-t*) curve (**Figure S6**) and long-term stability testing (**Figure S7**). The formate selectivity (~97%) of Au-Bi_2O_3 is amongst the highest recently reported for CO_2RR (**Table S1**), outperforming recent state-of-the-art catalysts. For instance, recent optimization of Bi-Sn bimetallic nanoparticles, defective Bi_2O_3 nanotubes derived Bi and eutectic Bi-Sn nanomaterials display formate selectivity of 94%, 94% and 78%, respectively.[8, 52, 53] Most notably, our Au-Bi_2O_3 fractal catalysts display one of the highest mass specific partial current density (-54 mA mg^{-1}) towards formate production amongst Bi-based catalysts, providing a more efficient material utilization. Furthermore, the scalability of the fractal synthesis approach developed here benefits the commercial large-scale production of these CO_2RR catalysts. In addition to demonstrating one of the highest FE_{HCOO^-}, the Au-Bi_2O_3 displays a very high mass-specific formate partial current density of -54 mA mg^{-1} which is higher than our previously reported one-step Bi_2O_3 (prepared using single flame spray pyrolysis method),[26] eutectic Bi-Sn (prepared using liquid alloy)[8] and Bi nanoflakes/nanosheets[54] catalysts. Unlike literature reported catalysts, this high selectivity and catalytic activity for CO_2 reduction alongside the one-step fabrication methods of stable and pure electrodes, without the use of binders and additional electrode preparation steps, bear significant potential for the commercial use of these Au-Bi_2O_3 fractals.

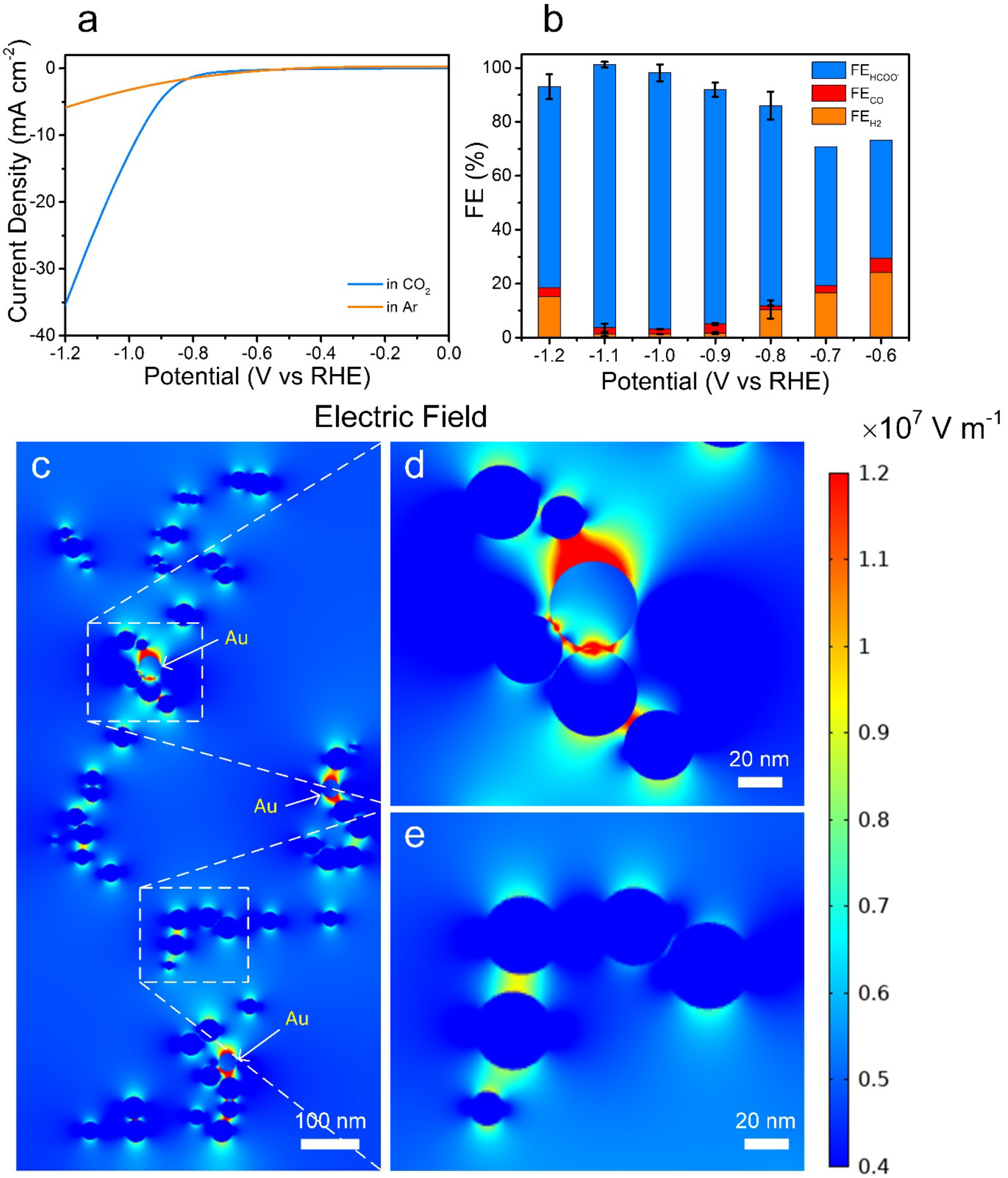

Figure 4. Electrochemical reduction of CO_2 with Au-Bi_2O_3. Dependence of (a) current density and (b) Faradaic efficiency on applied potentials in 0.1 M $KHCO_3$, and (c-e) Finite-element method (FEM) simulation results demonstrating the distribution of the electric field on the 2D projected area of the Au-Bi_2O_3 fractal with and applied potential of -3.0 V.

We propose that the active sites for formate generation within the Au-Bi_2O_3 fractals are a combination of (i) Bi_2O_3/Bi interfaces and (ii) roughened grain boundaries. As shown in **Figure S8**, the Bi_2O_3 layers undergo a partial reduction to form exposed Bi on the surface of Bi_2O_3 layers. These Bi sites are reported to lower the binding energy for *OCHO radicals, allowing the attainment of higher FE_{HCOO^-}.[52, 55] Further, the addition of a suitable amount of electronegative Au to Bi_2O_3 will result in suitable modification of surface electronic state of Bi, making it more active towards formate production. [56-58]. Similarly, the presence of roughened edges and grain boundaries is known to assist CO_2RR due to their complimentary electronic and chemical properties such as favourable adsorption of CO_2RR reaction intermediates.[59-61] Specifically, the high density of defects and grain boundary terminations present in these '*oxide-derived*' interface catalysts are already shown to display high CO_2RR activity.[59, 62] Post-reaction characterizations reveal that while the fractal structures are retained, the application of negative bias during CO_2RR results in more roughening of the catalyst surface, and thus in an increase in active sites for formate generation (**Figure S8**). Interestingly, post-reaction XPS characterization (**Figure S9**) with Au-Bi_2O_3 did not reveal the reduction of Bi_2O_3 to metallic bismuth, suggesting that the Au-Bi_2O_3 fractal electrodes are prone to rapid re-oxidation.[52]

On the basis of these findings, the improved CO_2RR activity, in terms of selectivity and current density, of the Au-Bi_2O_3 over previously reported Bi_2O_3 (**Figure S5a**) catalyst[26] is tentatively attributed to the enhancement of electron density by the presence of Au. Higher electron densities allow faster electron transport from the electrode to the CO_2 reactant molecules. To confirm this hypothesis, we carried out a series of experiments: (i) electron impedance spectroscopy (EIS), (ii) Mott-Schottky measurements (MS), and (iii) electron paramagnetic resonance (EPR) studies. Our EIS measurements reveal that the conductivity of the Bi_2O_3 improves as a result of Au addition (**Figure S10a**). This observation is further validated by the MS measurements, which indicate that Au-Bi_2O_3 possesses 5 times more electron donor density than that of the Bi_2O_3 without Au (**Figure S10b,c**). Lastly, the EPR studies (**Figure S11**) indicate that the addition of Au results in an increase in unpaired electrons that are trapped by Au-Bi_2O_3, as indicated by the sharp EPR peak intensity at $g = 2.09$.[63, 64] Collectively, these results indicate that the improved electron density of the Au-Bi_2O_3 enables faster electron transfer to the CO_2 molecules resulting in the generation of $*CO_2^{\cdot -}$ radical intermediates. The latter radicals are considered as the rate determining step, followed by proton and electron transfer to generate formate through either *OCHO or *COOH intermediates.[30, 65, 66] To further understand how this variation in electron density affects the CO_2RR activity, we simulated the electric field distribution of the catalyst using a finite element method (FEM). It can be observed from **Figure 4c-e** that in the absence of Au, the electric field within the Bi_2O_3 is homogenous whereas the addition of Au leads to bright spots, indicating a very strong electric field as a result of higher free electron density.[67] These '*hot edges*' corresponding to strong electric fields are reported to be beneficial for CO_2RR, owing to the faster electron transfer from these sites to the CO_2 reactants.[68, 69] Moreover, these strong electric field spots assist in concentrating electrolyte cations near the active sites, resulting in high local concentration of CO_2 by reducing the mean square displacement of CO_2 to the catalyst surface and thereby promoting faster reaction kinetics.[67, 70]

A systematic investigation of the Au impact on the formate production performance was carried out by varying the amount of Au loading between 1 and 10 wt. %. Increasing the Au content within the Au-Bi_2O_3 leads to improved conductivity (**Figure S10a**), increased electron density (**Figure S10b,c**) and pronounced "*hot edges*" (**Figure S12**), however, this also corresponded to an increase in Au particle size **(Figure S13**). The CO_2RR tests as a function of the Au content reveal that increasing the Au loading from 1 to 10% leads to an increase in overall current density (**Figure S14**) from -9 to -25 mA cm^{-2} and a decrease of formate selectivity from 97 to 70% by increasing the selectivity of CO and H_2 (**Figure S15**). Specifically, increasing the Au loading from 1% to 10% increases the FE_{CO} from 0.5% to 25%. This is in agreement with our control experiments with pure Au on CFP (**Figure S5b**) that reveals that Au is capable of generating only H_2 and CO during CO_2RR.[71] These results indicate that at low Au content ($\leq$ 5%), the Au nanoparticles do not play a major role in governing the CO_2RR activity. At these low Au loading, the fractional exposure of the Au nanoparticle surface to the CO_2RR reactants is limited, thereby suppressing CO formation.[72,73] Rather, providing a suitable amount of electronegative Au to Bi_2O_3 will lead to favorable modification of the electronic structure of Bi, making it more active towards formate production.[53,57,74] Subsequently, increasing the Au content beyond the optimal loading increases the fraction of Au nanoparticles, promoting the formation of CO selective facets and thus CO during CO_2RR. Further, to rule out the effect of quantitative change in active sites within the Au-Bi_2O_3 catalysts due to Au addition, we carried electrochemical active surface area (ECSA) measurements (**Figure S16**), which revealed similar ECSA for all the catalysts. These results indicate that Au does not contribute to an increase density of active sites but in tuning the Bi electronic structure, and an optimal content of 5% Au for CO_2RR to formate generation.

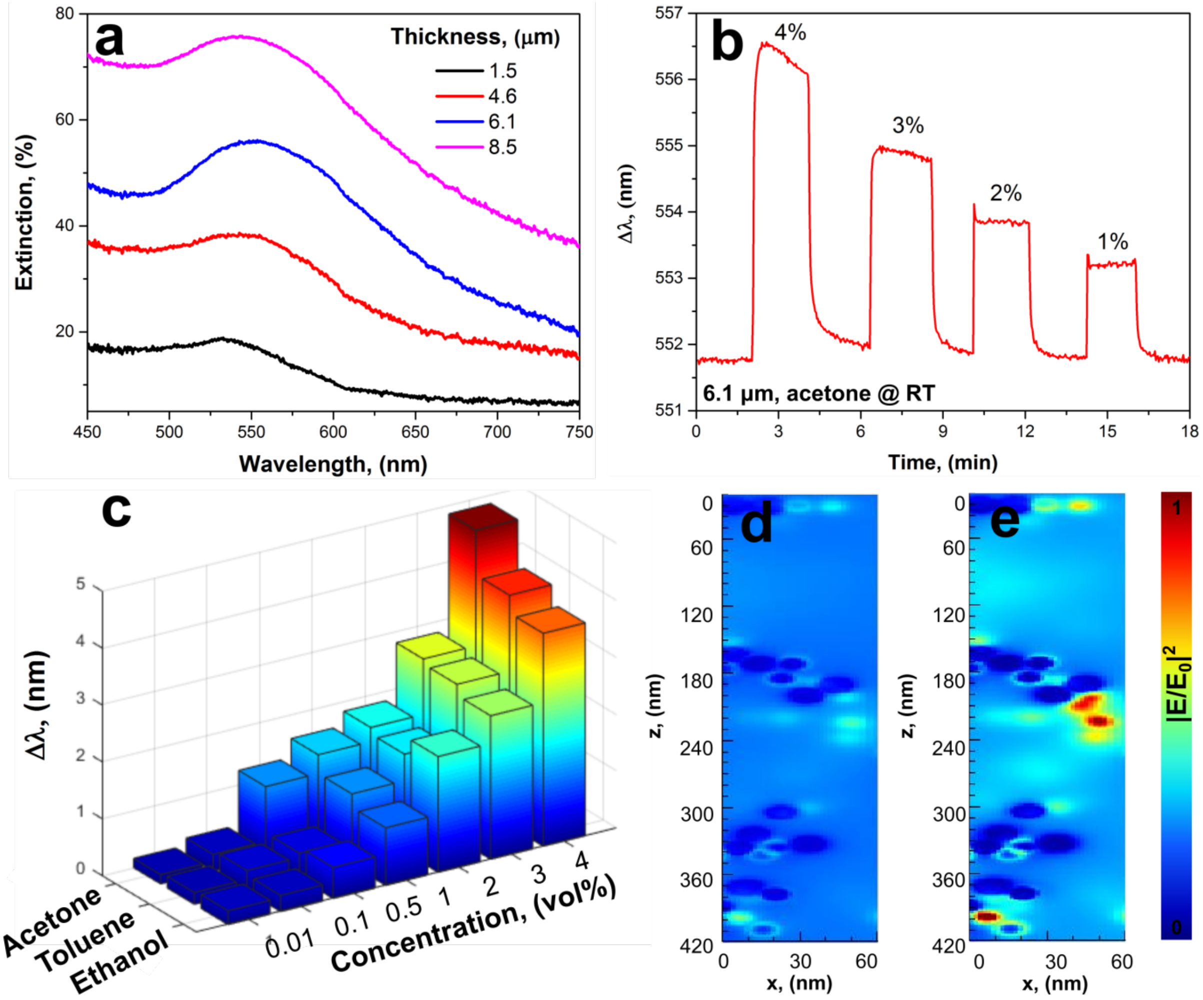

Figure 5. Optical characterization and gas sensing. (a) Extinction measurements in the visible range for the 3D fractal metamaterials with different thicknesses. (b) Plasmonic wavelength shift upon different on/off injection cycles of acetone with different concentrations at room temperature. (c) Summary of the sensing results for different volatile organic compounds at various concentrations. (d) Exemplary electric-field distribution for a Bi_2O_3 fractal with $D_f = 1.80$ and (e) the Bi_2O_3 fractal with embedded Au nanoparticles.

Furthermore, the integration of gold nanocrystals within the fractal scaffold –other than improving the catalytic performance– has important consequences in the confinement of the electromagnetic field into three-dimensionally distributed subwavelength regions. Indeed, by shining electromagnetic radiation of suitable frequency, the free electron gas density of the metallic scatters starts to collectively oscillate giving a rise to a plasmonic response which drastically influences the optical properties of the material.[75] Due to the strong light coupling of the Au nanoparticles, a characteristic pink coloration is present in all the considered samples (**Figure S1**). **Figure 5a** shows the far-field optical properties of our Au-Bi_2O_3 metamaterials for different thicknesses (**Figure S17**).

Despite the absorptive behavior of Bi_2O_3 at wavelengths shorter than ~ 430 nm ($E_g = 2.85$ eV), the ultra-high hierarchical porosity of the structure drastically reduces the scattering and provides a way to maintain an overall excellent transparency in the visible range, up to ~10 µm.[76] A resonance band in the extinction spectra of the 3D Au crystal is observed in the range of 500-600 nm independent of the thickness. The latter arises from the d-band of the plasmonic Au nanoparticles. The spectra show a gradual intensity increase and a little broadening and red-shift as the fractal film thickness increases. This is attributed to the rise of photonic modes driven by the mesoscale-size of the fractal film.[77]

A peculiar characteristic of plasmonic structures is their intrinsic ability to respond to variations in local refractive index and transduce them into spectral shifts. This has been widely exploited for sensing applications, with particular focus on the detection of analytes in liquid or physiological environments.[75, 78, 79] By employing different strategies, ranging from surface functionalization to fine optimization of the nanostructures, plasmonic sensors have been able to detect very low concentrations, in the femtomolar range,[80, 81] of biomarkers in liquid environment. However, translating these achievements to gas detection has been proven challenging for many reasons. Among them, the most important ones are the non-specific binding between the gases and the host plasmonic matrix, their high volatility and the small refractive index change induced by volatile compounds.[16] This last point is of utmost importance as very optimized sensors need to be developed to achieve these sensitivity levels.

Often, this is hindered by the inner physical phenomena associated with plasmon excitation. In fact, a drawback of highly absorbent metallic structures arises from the evanescent nature of the plasmonic field, which exponentially decays within a few tens of nm from the scattering center.[82] Hence, increasing the plasmonic active volume while maintaining the strong localization of the near-field enhancement will be tremendously impactful for sensing applications, and beyond. Our innovative fractal structure provides a novel alternative that helps to overcome these limitations. In fact, the three-dimensionally distributed Au nanocrystals provide an increased plasmonic active volume which is extremely beneficial for sensing essays.[83] Indeed, an increased active volume corresponds to drastic enhancement of the near-field, which will in turn provide higher sensitivity and will be tremendously impactful for sensing applications and beyond. Additionally, the Bi_2O_3 –Au fractals provide very high specific surface area, an ideal feature for gaseous molecule physisorption, which enables the room temperature detection of volatile organic compounds.

Here, we showcase the plasmonic sensing properties of our 3D fractal media by optical sensing of standard volatile organic compounds, namely acetone, toluene, and ethanol. **Figure 5b** shows typical dynamic sensing responses with an optimized fractal film structure, having a thickness of *ca.* 6.1 µm (**Figure 5a,** blue line) to successive room-temperature injections of decreasing concentrations of acetone, from 4 vol% to 1 vol%. The introduction of the acetone gas molecule on the fractal causes a change in the environmental refractive index (**Figure S18a,b**), which in turn shifts the plasmonic resonance wavelength, leading to shifts as high as *ca.* 5 nm for 4 vol%. The high porosity enables fast gas diffusion and adsorption, which in turn leads to a quick and reversible anchoring of the VOCs within the fractal system, with short response and recovery time, both in the order of 5s. It should be notice that although having a lower extinction compared to that of the 8.5 µm sample (**Figure 5a**, pink line), the sharper peak of the 6.1 µm thick sample leads to the better overall sensing performances with lower limit of detection and higher sensitivity (**Figure S18c**).[79, 84]

Furthermore, to validate the sensing performance of the 3D fractal media, other volatile gases were sensed with the Bi_2O_3-Au fractals. The change in the VOC presence and concentration resulted in a redshift of the resonance frequency, which is in line with the increase of the refractive index from pure air to the VOC containing atmosphere. The magnitude of the redshift was dependent on the gas molecule and its concentration (**Figure 5c**). Despite the lower refractive index of acetone, the Au-Bi_2O_3 fractals show a stronger response toward acetone than to the other two VOCs. This is possibly attributed to the different binding energy and higher affinity of acetone to the Bi_2O_3 surface as recently reported.[85] Notably, acetone concentrations as low as 0.01 vol% at room temperature, corresponding to a refractive index change of $< 8 \times 10^{-7}$, were measured proving the highly sensitive detection ability of the Au-Bi_2O_3 fractals.

A set of finite-difference time domain (FDTD) simulations on realistic systems, comprising of Bi_2O_3 fractal cluster with $D_f = 1.8$ obtained with a diffusion limited aggregation algorithm,[86] and on the same system including 5% Au nanoparticles scattered though the 3D fractal were performed. Upon white-light interaction, the pure Bi_2O_3 semiconductor shows little interaction in the visible range resulting in an almost nil near-field enhancement ($|\mathbf{E}/\mathbf{E_0}|^2$), as shown in the representative electric-field distribution taken at $\lambda = 540$ nm of **Figure 5d**. The addition of distributed plasmonic Au particles results in a much stronger coupling with the incoming light, leading to a multitude of three-dimensionally scattered *hot-spots* in which the electric field is greatly enhanced (**Figure 5e**). Similar to the finite-element method (FEM) simulation results, these *hot-spots* are of utmost importance, not only for catalytic reactions but also for sensing purposes,[87] as those regions are the most sensitive to changes in refractive index and their distribution in the *x-y-z* space provides a superior way to enhance the sensing essay volume and reaching extraordinary low limits of detection, with magnitude of shifts comparable to the one in liquid environments with label free plasmonics systems.[88]

The linear dependency of the LSPR resonance with the medium permittivity has been broadly used to detect bio-chemical molecules in liquid or physiological environments.[16, 75] However, the translation of these achievements to gas molecules has been proven to challenging. The reason relies on the very minute changes in the refractive index induced by gas molecules. For instance, a pure gas acetone environment has a refractive index of 1.001090, while pure air is 1.000293,[89] resulting in a refractive index variation in the order of 10^{-3}. In this context, our fractal Au-Bi_2O_3 materials extend the current LSPR limit of detection for gas molecules by more than one order of magnitude achieving detection of down to 100 ppm of acetone in air. While this is still insufficient for application in breath analysis of acetone for diabetes diagnostics, detection of volatile organic compounds in this concentration range is still useful for various environment monitoring applications. For instance, 1000 ppm of acetone in air may cause uncomfortable symptoms including headache, fatigue, dizziness and even narcosis.[90] Additionally, a threshold value of 2.6 vol% is considered the flammable limit for acetone.[91] As such, our Au-Bi_2O_3 fractals could be used for optical monitoring of the air quality in industrial environments, where acetone and other organic solvents are heavily used.[92]

Conclusion

Herein, we report the design and development of a multifunctional hetero-nanostructured Au-Bi_2O_3 fractal with a uniform distribution of Au and Bi_2O_3 particles by one-step hot-aerosol synthesis. We confirm the fractal nature of the material through image analysis and synchrotron-based experimental approaches, and reveal that the fractal dimension of the structure is ≈ 1.80. The as-prepared unique 3D fractal structure of the Au-Bi_2O_3 nanohybrid was then applied to a range of applications such as CO_2 reduction and optical gas sensing, displaying very high activity. For CO_2RR, the fractal structure displayed a high selectivity towards the formation of formate, achieving a very high FE_{HCOO^-} of 97% alongside a high mass-specific formate partial current density of -54 mA mg^{-1} at -1.1 V vs RHE. When used for optical gas sensing, this structural material shows a strong enhancement in the localized electric field, resulting in a plasmonic shift as high as ~ 5 nm for 4 vol% of the acetone sensing with a detection limit of 100 ppm towards different VOCs. The excellent performances of the fractal Au-Bi_2O_3 structure are attributed to (i) the homogeneous arrangement of Au and Bi_2O_3 components in the 3D structure, leading to the enhancement in electron density and plasmonic active volume driven from the Au nanoparticles, (ii) the high surface area with abundance active sites for CO_2 and VOCs adsorption. The design guidelines and engineering applicability demonstrated by these fractal structures can be extended to other nanomaterials and applications such as in energy storage and conversion.

Experimental

Fabrication of Au-Bi_2O_3: Au-Bi_2O_3 nanoparticle aerosols were prepared by modifying a recently reported procedure for Au-TiO_2 aerosols with a double custom-built flame spray pyrolysis (DFSP) system, which consisting of two separate nozzles: one used for feeding Bi_2O_3 liquid precursor and the other used for feeding Au liquid precursor.[93] Briefly, a Bi_2O_3 precursor solution, consisting of bismuth(III) 2-ethylhaxnoate (70-75% in xylenes, 24% Bi, Strem) was dissolved in a 1:1 (vol.) mixture of toluene (anhydrous 99.8%, Sigma-Aldrich) and 2-ethylhexanoic acid (99%, Sigma-Aldrich) to achieve concentrations of 0.2 M (metal precursor concentration). The Au precursor solution, containing gold(III) chloride trihydrate (Sigma-Aldrich), was dissolved in ethyl alcohol (anhydrous, Sigma-Aldrich) to form 0.01 M solution (5 mol% of Au). Both solutions were fed at 3 mL min^{-1} through to the DFSP system by syringe pumps and atomized with oxygen flow (5 L min^{-1}, BOC grade 2.5) at a constant pressure drop of 4 bar. The resulting spray was ignited with a surrounding annular set of premixed methane/oxygen flame (CH_4-flamelet 1.8 L min^{-1}, O_2-flamelet 2.0 L min^{-1}, COREGAS grade 4.5). The Au-Bi_2O_3 films were fabricated by DFSP of the precursors directly on either carbon paper (Toray Paper TGP-H-120) for CO_2RR or a transparent glass substrate for optical gas sensing. The height above burner (HAB) was 17 cm. Bi_2O_3 on CFP without Au nanoparticles and Au on CFP without Bi_2O_3 were also fabricated for comparison. Different gold concentrations (0.005 M and 0.02 M, corresponding to 1 mol% and 10 mol% of Au respectively) were also prepared for comparison. The 1-channel type K thermometer (Testo 925) with an immersion tip, flexible, TC type K probe was placed in front of the substrates to measure the exposed temperature during the synthesis.

Material Characterization

The morphology of the FSP Au-Bi_2O_3 films were investigated using a field-emission scanning electron microscope (FESEM) Zeiss Ultraplus operating at 3 kV without coating, and a high-resolution transmission electron microscope (TEM) JEOL 2100F at 200 kV. The FESEM is equipped with standard secondary electron and angle-sensitive backscattering detectors. Samples for SEM were prepared by fixing the cut pieces of the electrode on the specimen stubs using carbon tape. Samples for TEM were prepared by scratching the material from the electrode surface and dispersing on holey carbon coated 200 mesh copper grids. X-ray diffraction (XRD) patterns were recorded using a D2 Phaser Bruker system with Cu Kα radiation of average wavelength 1.54059 Å at a scan rate of 1.17 deg min^{-1}. XRD of the Au-Bi_2O_3 was measured on the glass. Thermogravimetric analysis (TGA) of the Au-Bi_2O_3 (5% Au) powder (13.22 mg) was carried out by NETZSCH STA 449 F3 Jupiter analyzing instrument in the temperature range of 58–700 °C. X-ray photoelectron spectroscopy (XPS) of the Au-Bi_2O_3 before and post CO_2RR tested were carried out using Thermo ESCALAB250Xi X-ray photoelectron spectrometer with monochromated Al K alpha (energy 1486.68 eV) as the X-ray source. The pass energy was 100 eV for survey scans and 20 eV for region scans. Au 4f7/2, Ag 3d5/2 and Cu 2p3/2 were used to calibrate the instrument. Fractal analysis of the Au-Bi_2O_3 films was done using ImageJ software with an open-source plugin, namely FracLac.[16, 25, 26, 94] Details of the analysis were presented in the supporting information. Electron paramagnetic resonance (EPR) spectroscopy was carried out on a Bruker EMX‐plus X‐Band EPR spectrometer. The EPR measurements were conducted at 9.41 GHz (X‐band) at 120 K with the microwave power set at 2 mW and the modulation amplitude at 5G. SAXS measurements were performed at the SAXS/WAXS beamline of the Australian Synchrotron in Melbourne, Australia in transmission mode with a photon energy of 12 keV and a sample to detector length of approximately 7.2 m. The images were recorded using a 2-dimensional Pilatus 1M hybrid pixel detector using exposure times between 0.5 and 5 seconds. Accurate calibration of the q range was done for each group of measurements using a Silver Behenate (AgBeh) standard.

Electrochemical Reduction of CO_2

All electrochemical measurements in this study were carried out with a CHI 760E (CH Instrument, Texas) electrochemical workstation using a customized gas-tight two compartment (separated by a glass frit) H-cell. The cathodic compartment of the cell contained the Au-Bi_2O_3 electrodes and a saturated calomel electrode (SCE) as the working and reference electrode, respectively whereas the anode compartment contained a Pt wire as the counter electrode. The electrolyte utilized in this study for CO_2 reduction was 0.1 M $KHCO_3$. Preceding each experiment, the cathodic compartment of the H-cell was purged with CO_2 for 30 minutes, and the saturated 0.1 M $KHCO_3$ solution gave a pH measurement of 6.8. All potentials measured in this study were converted to the reversible hydrogen electrode (RHE) reference for the purpose of comparison, using the following equation: E_{RHE} (V) = E_{SCE} (V) + 0.245 + 0.059 × pH. Potentiostatic studies were carried out at various potentials for duration of 1 h. The impedance electron spectroscopy (EIS), Mott-Schottky (MS), and relative electrochemically active surface area (ECSA) measurements were carried out in 0.5 M Na_2SO_4 solution pH 6.8. EIS was measured under -0.4 V vs RHE with the frequency from 100 kHz to 0.1 Hz, and MS was measured at frequency of 1 kHz at applied potential window ranging from -1.2 to 0 V vs RHE. The cyclic voltammetry of different samples in the potential range of 0.61 to 0.81 V vs RHE was recorded at different scan rates. Then the electrochemical capacitance current at potential of 0.7 V vs RHE of each sample was used to evaluate the ECSA.[95]

Product Analysis

The gas phase products were quantified using a gas chromatograph (Shimadzu, Model 2010 plus), equipped with both a thermal conductivity detector (TCD) and flame ionization detector (FID). Liquid products were analyzed using a 600 MHz ^1H 1 D liquid NMR spectrometer (Bruker Advance) at 25°C. Typically, 0.5 mL of liquid sample was collected at the end of each experiment and was mixed with 0.1 mL of D_2O and 7.143 ppm of internal standard dimethyl sulfoxide (DMSO, Sigma 99.99%). The 1D ^1H spectrum was measured with water suppression with a pre-saturation method. The quantities of products were calculated by comparing the integral areas of an observed liquid product with that of the DMSO.

Growth modeling

The Bi_2O_3 fractals were generated through a custom made Matlab code based on the diffusion limited aggregation in three dimensions. The cluster chosen to mimic the experimental result is composed of 500 nanoparticles of diameter and has a $D_f = 1.84$.

Finite-element method (FEM) simulation

Electric field distribution of the simplified 2D model of the Au-Bi_2O_3 fractal was generated using COMSOL Multiphysics with the Electrostatics module. Firstly, 2D projection of the Bi_2O_3 fractal was created in a region of 640 × 320 nm. Then, gold nanoparticles were added into the model. Relative permittivity of the H_2O, Bi_2O_3 and Au were chosen to be 1.77, 2.5, and -5.8 + 2.1i, respectively. A potential of -3.0 V and 0 V were applied on the 2D model as shown in **Figure S19**.

Finite-different time-domain (FDTD) simulation

Optical simulations were performed with commercially available software (Lumerical FDTD) which is based on finite-difference time-domain (FDTD). Perfectly matched layers were employed as boundary conditions to avoid the wave reflection at the boundary. A total-field scattered-field source with a polarization along the x-axis and a propagation vector along the z-direction was chosen to excite from the backside of the structure. A nonuniform meshing refinement was used to guarantee a precise result with a smallest mesh cell of 0.2 nm to increase the accuracy of the simulation. The near-field enhancements at the resonance were then monitored using a set of frequency domain probes.

Optical Gas Sensing Measurement

The sensing measurements were conducted through a transmittance optical setup equipped with a Vis halogen lamp which is focused onto a customized sensing chamber via a series of adjustable apertures and collimating and objective lenses. The transmitted light is then collected and transported via an optical fiber into a UV-Vis modular spectrometer from Ocean Optics, Flame-S-XR1-ES which is connected to a desktop through a USB port. A resonance band in the extinction spectra was evaluated as Extinction (%) =100 - Transmittance (%). A gas delivery system with controlled flow rate is integrated on the optical setup and to deliver the gases in the chamber. The transmittance is monitored in real time, and a spectrum is sampled every two seconds. Post analysis and sensing response plots were carried out with a centroid algorithm[96] to track the plasmonic shift.

Conflicts of interest

There are no conflicts to declare

Author Contribution

T.T., R.D., Z.F., R.A., and A.T. conceived the concept, designed, directed the research and co-wrote the manuscript. T.T. and Z.F. conducted material synthesis and simulations, R.D. and T.T. carried out electrochemical experiments. Z.F. and L.A.R. performed optical measurements. T.T., R.D., Z.M., A.K., P.K., X.G. H.C., and Y.Z. carried out material characterization, synchrotron experiments and associated analysis. All authors discussed the results and contributed to the the final version of the manuscript.

Electronic Supplementary Information (ESI) available:

Acknowledgements

Authors acknowledge the financial supports of the Australian Research Council (ARC) DP150101939, ARC DE160100569, ARC Research Hub on Integrated Energy Storage Solutions, Westpac 2016 Research Fellowship, and the Research School of Engineering of the ANU. Authors also acknowledge the Centre for Advanced Microscopy (CAM) with funding through the Australian Microscopy and Microanalysis Research Facility (AMMRF). R.D. & R.A. would like to acknowledge funding from the UNSW Digital Grid Futures Institute. T.T also thanks Dr. Felipe Kremer for the assistance with the TEM measurement at CAM. Part of the research was undertaken at the SAXS/WAXS beamline at the Australian

Synchrotron, part of ANSTO, and we thank the beamline scientists for their technical assistance.

References

1. Y. Lee, J. Park, A. Choe, S. Cho, J. Kim and H. Ko, *Adv. Funct. Mater.*, 2019, 1904523.
2. T. Khudiyev, T. Dogan and M. Bayindir, *Scientific Reports*, 2014, **4**, 4718.
3. Y. Liu, X. Chen and J. Xin, *Bioinspiration & biomimetics*, 2008, **3**, 046007.
4. J. Zi, X. Yu, Y. Li, X. Hu, C. Xu, X. Wang, X. Liu and R. Fu, *Proceedings of the National Academy of Sciences*, 2003, **100**, 12576-12578.
5. A. Cao, V. P. Veedu, X. Li, Z. Yao, M. N. Ghasemi-Nejhad and P. M. Ajayan, *Nature Materials*, 2005, **4**, 540-545.
6. M. Khorasaninejad and F. Capasso, *Science*, 2017, **358**, eaam8100.
7. M. Ahmaruzzaman, D. Mohanta and A. Nath, *Scientific Reports*, 2019, **9**, 12935.
8. J. Tang, R. Daiyan, M. B. Ghasemian, S. A. Idrus-Saidi, A. Zavabeti, T. Daeneke, J. Yang, P. Koshy, S. Cheong, R. D. Tilley, R. B. Kaner, R. Amal and K. Kalantar-Zadeh, *Nature Communications*, 2019, **10**, 4645.
9. V. Narasimhan, R. H. Siddique, J. O. Lee, S. Kumar, B. Ndjamen, J. Du, N. Hong, D. Sretavan and H. Choo, *Nature Nanotechnology*, 2018, **13**, 512-519.
10. X. Li, F. Gong, D. Liu, S. He, H. Yuan, L. Dai, X. Cai, J. Liu, J. Guo, Y. Jin and F. Sang, *Org. Electron.*, 2019, **69**, 216-219.
11. T. W. Kim and K.-S. Choi, *Science*, 2014, **343**, 990-994.
12. S. C. Warren, K. Voïtchovsky, H. Dotan, C. M. Leroy, M. Cornuz, F. Stellacci, C. Hébert, A. Rothschild and M. Grätzel, *Nature Materials*, 2013, **12**, 842.
13. D. S. Wiersma, *Nature Photonics*, 2013, **7**, 188-196.
14. H. Yin, B. Dong, X. Liu, T. Zhan, L. Shi, J. Zi and E. Yablonovitch, *Proceedings of the National Academy of Sciences*, 2012, **109**, 10798-10801.
15. L. Cortese, L. Pattelli, F. Utel, S. Vignolini, M. Burresi and D. S. Wiersma, *Advanced Optical Materials*, 2015, **3**, 1337-1341.
16. Z. Fusco, M. Rahmani, R. Bo, R. Verre, N. Motta, M. Käll, D. Neshev and A. Tricoli, *Adv. Mater.*, 2018, **30**, 1800931.
17. J. van den Broek, S. Abegg, S. E. Pratsinis and A. T. Güntner, *Nature Communications*, 2019, **10**, 4220.
18. B. B. Mandelbrot, *The fractal geometry of nature*, WH freeman New York, 1983.
19. M. A. McEvoy and N. Correll, *Science*, 2015, **347**, 1261689.
20. J. A. Fan, W.-H. Yeo, Y. Su, Y. Hattori, W. Lee, S.-Y. Jung, Y. Zhang, Z. Liu, H. Cheng, L. Falgout, M. Bajema, T. Coleman, D. Gregoire, R. J. Larsen, Y. Huang and J. A. Rogers, *Nature Communications*, 2014, **5**, 3266.
21. K. Li, M. I. Stockman and D. J. Bergman, *Phys. Rev. Lett.*, 2003, **91**, 227402.
22. R. Kopelman, *Science*, 1988, **241**, 1620-1626.
23. N. Kenkel and D. Walker, *Coenoses*, 1996, 77-100.
24. S. Shibuichi, T. Onda, N. Satoh and K. Tsujii, *The Journal of Physical Chemistry*, 1996, **100**, 19512-19517.
25. B. Fazio, P. Artoni, M. Antonia Iatì, C. D'Andrea, M. J. Lo Faro, S. Del Sorbo, S. Pirotta, P. Giuseppe Gucciardi, P. Musumeci, C. Salvatore Vasi, R. Saija, M. Galli, F. Priolo and A. Irrera, *Light: Science & Applications*, 2016, **5**, e16062-e16062.
26. T. Tran-Phu, R. Daiyan, Z. Fusco, Z. Ma, R. Amal and A. Tricoli, *Adv. Funct. Mater.*, **0**, 1906478.
27. R. Strobel, L. Mädler, M. Piacentini, M. Maciejewski, A. Baiker and S. E. Pratsinis, *Chem. Mater.*, 2006, **18**, 2532-2537.
28. M. Høj, D. K. Pham, M. Brorson, L. Mädler, A. D. Jensen and J.-D. Grunwaldt, *Catal. Lett.*, 2013, **143**, 386-394.
29. R. Daiyan, E. C. Lovell, N. M. Bedford, W. H. Saputera, K.-H. Wu, S. Lim, J. Horlyck, Y. H. Ng, X. Lu and R. Amal, *Adv. Sci*, 2019, **0**, 1900678.
30. R. Daiyan, X. Lu, Y. H. Ng and R. Amal, *ChemSusChem*, 2017, **10**, 4342-4358.

31. C.-T. Dinh, T. Burdyny, M. G. Kibria, A. Seifitokaldani, C. M. Gabardo, F. P. García de Arquer, A. Kiani, J. P. Edwards, P. De Luna, O. S. Bushuyev, C. Zou, R. Quintero-Bermudez, Y. Pang, D. Sinton and E. H. Sargent, *Science*, 2018, **360**, 783-787.
32. M. Tepluchin, D. K. Pham, M. Casapu, L. Mädler, S. Kureti and J.-D. Grunwaldt, *Catalysis Science & Technology*, 2015, **5**, 455-464.
33. E. C. Lovell, H. Großman, J. Horlyck, J. Scott, L. Mädler and R. Amal, *ACS Appl. Mater. Interfaces*, 2019, **11**, 25766-25777.
34. E. Goudeli, M. L. Eggersdorfer and S. E. Pratsinis, *Langmuir*, 2015, **31**, 1320-1327.
35. F. Pierce, C. M. Sorensen and A. Chakrabarti, *Physical Review E*, 2006, **74**, 021411.
36. N. Nasiri, R. Bo, F. Wang, L. Fu and A. Tricoli, *Adv. Mater.*, 2015, **27**, 4336-4343.
37. R. Kubrin, A. Tricoli, A. Camenzind, S. E. Pratsinis and W. Bauhofer, *Nanotechnology*, 2010, **21**, 225603.
38. B. Fazio, P. Artoni, M. A. Iatì, C. D'andrea, M. J. L. Faro, S. Del Sorbo, S. Pirotta, P. G. Gucciardi, P. Musumeci and C. S. Vasi, *Light: Science & Applications*, 2016, **5**, e16062.
39. G. Beaucage, *J. Appl. Crystallogr.*, 1995, **28**, 717-728.
40. J. Hyeon-Lee, G. Beaucage, S. E. Pratsinis and S. Vemury, *Langmuir*, 1998, **14**, 5751-5756.
41. A. J. Gröhn, S. E. Pratsinis, A. Sánchez-Ferrer, R. Mezzenga and K. Wegner, *Industrial & Engineering Chemistry Research*, 2014, **53**, 10734-10742.
42. M. L. Eggersdorfer, D. Kadau, H. J. Herrmann and S. E. Pratsinis, *Langmuir*, 2011, **27**, 6358-6367.
43. M. L. Eggersdorfer, D. Kadau, H. J. Herrmann and S. E. Pratsinis, *J. Aerosol Sci*, 2012, **46**, 7-19.
44. C. Sorensen, *Aerosol Sci. Technol.*, 2011, **45**, 765-779.
45. G. Bushell, Y. Yan, D. Woodfield, J. Raper and R. Amal, *Adv. Colloid Interface Sci.*, 2002, **95**, 1-50.
46. T. Li, A. J. Senesi and B. Lee, *Chem. Rev.*, 2016, **116**, 11128-11180.
47. H. K. Kammler, G. Beaucage, R. Mueller and S. E. Pratsinis, *Langmuir*, 2004, **20**, 1915-1921.
48. T. W. Kim and K.-S. Choi, *Science*, 2014, **343**, 990-994.
49. H.-Y. Jiang, P. Li, G. liu, J. Ye and J. Lin, *J. Mater. Chem. A*, 2015, **3**, 5119-5125.
50. D. Gao, Y. Zhang, Z. Zhou, F. Cai, X. Zhao, W. Huang, Y. Li, J. Zhu, P. Liu and F. Yang, *JACS*, 2017, **139**, 5652-5655.
51. V. S. Dharmadhikari, S. Sainkar, S. Badrinarayan and A. Goswami, *J. Electron. Spectrosc. Relat. Phenom.*, 1982, **25**, 181-189.
52. Q. Gong, P. Ding, M. Xu, X. Zhu, M. Wang, J. Deng, Q. Ma, N. Han, Y. Zhu, J. Lu, Z. Feng, Y. Li, W. Zhou and Y. Li, *Nature Communications*, 2019, **10**, 2807.
53. G. Wen, D. U. Lee, B. Ren, F. M. Hassan, G. Jiang, Z. P. Cano, J. Gostick, E. Croiset, Z. Bai and L. Yang, *Adv. Energy Mater.*, 2018, **8**, 1802427.
54. W. Zhang, Y. Hu, L. Ma, G. Zhu, P. Zhao, X. Xue, R. Chen, S. Yang, J. Ma and J. Liu, *Nano energy*, 2018, **53**, 808-816.
55. N. Han, Y. Wang, H. Yang, J. Deng, J. Wu, Y. Li and Y. Li, *Nature communications*, 2018, **9**, 1320.
56. X. Bai, W. Chen, C. Zhao, S. Li, Y. Song, R. Ge, W. Wei and Y. Sun, *Angew. Chem. Int. Ed.*, 2017, **56**, 12219-12223.
57. W. Luc, C. Collins, S. Wang, H. Xin, K. He, Y. Kang and F. Jiao, *JACS*, 2017, **139**, 1885-1893.
58. G. Wen, D. U. Lee, B. Ren, F. M. Hassan, G. Jiang, Z. P. Cano, J. Gostick, E. Croiset, Z. Bai, L. Yang and Z. Chen, *Adv. Energy Mater.*, 2018, **8**, 1802427.
59. X. Feng, K. Jiang, S. Fan and M. W. Kanan, *JACS*, 2015, **137**, 4606-4609.
60. C. W. Li, J. Ciston and M. W. Kanan, *Nature*, 2014, **508**, 504.
61. X. Feng, K. Jiang, S. Fan and M. W. Kanan, *ACS Central Science*, 2016, **2**, 169-174.
62. R. G. Mariano, K. McKelvey, H. S. White and M. W. Kanan, *Science*, 2017, **358**, 1187-1192.
63. D. Barreca, F. Morazzoni, G. A. Rizzi, R. Scotti and E. Tondello, *PCCP*, 2001, **3**, 1743-1749.
64. S. Chen, H. Wang, Z. Kang, S. Jin, X. Zhang, X. Zheng, Z. Qi, J. Zhu, B. Pan and Y. Xie, *Nature Communications*, 2019, **10**, 788.

65. I. V. Chernyshova, P. Somasundaran and S. Ponnurangam, *Proceedings of the National Academy of Sciences*, 2018, **115**, E9261-E9270.
66. R. Daiyan, W. H. Saputera, H. Masood, J. Leverett, X. Lu and R. Amal, *Adv. Energy Mater.*, **n/a**, 1902106.
67. C. Chen, Y. Pang, F. Zhang, J. Zhong, B. Zhang and Z. Cheng, *J. Mater. Chem. A*, 2018, **6**, 19621-19630.
68. Y. Yang, L. Ohnoutek, S. Ajmal, X. Zheng, Y. Feng, K. Li, T. Wang, Y. Deng, Y. Liu, D. Xu, V. K. Valev and L. Zhang, *J. Mater. Chem. A*, 2019, **7**, 11836-11846.
69. M. Morimoto, Y. Takatsuji, K. Hirata, T. Fukuma, T. Ohno, T. Sakakura and T. Haruyama, *Electrochim. Acta*, 2018, **290**, 255-261.
70. M. Liu, Y. Pang, B. Zhang, P. De Luna, O. Voznyy, J. Xu, X. Zheng, C. T. Dinh, F. Fan and C. Cao, *Nature*, 2016, **537**, 382.
71. T. Saberi Safaei, A. Mepham, X. Zheng, Y. Pang, C.-T. Dinh, M. Liu, D. Sinton, S. O. Kelley and E. H. Sargent, *Nano Lett.*, 2016, **16**, 7224-7228.
72. D. Kim, J. Resasco, Y. Yu, A. M. Asiri and P. Yang, *Nature Communications*, 2014, **5**, 4948.
73. Z. Tao, Z. Wu, X. Yuan, Y. Wu and H. Wang, *ACS Catalysis*, 2019, **9**, 10894-10898.
74. X. Bai, W. Chen, C. Zhao, S. Li, Y. Song, R. Ge, W. Wei and Y. Sun, *Angew. Chem. Int. Ed.*, 2017, **56**, 12219-12223.
75. A. Tittl, H. Giessen and N. Liu, *Nanophotonics*, 2014, **3**, 157-180.
76. A. Tricoli and S. E. Pratsinis, *Nature Nanotechnology*, 2010, **5**, 54-60.
77. S. Y. Park, J.-S. Lee, D. Georganopoulou, C. A. Mirkin and G. C. Schatz, *The Journal of Physical Chemistry B*, 2006, **110**, 12673-12681.
78. J. N. Anker, W. P. Hall, O. Lyandres, N. C. Shah, J. Zhao and R. P. Van Duyne, in *Nanoscience and Technology: A Collection of Reviews from Nature Journals*, World Scientific, 2010, pp. 308-319.
79. Z. Fusco, M. Rahmani, R. Bo, T. Tran-Phu, M. Lockrey, N. Motta, D. Neshev and A. Tricoli, *Adv. Funct. Mater.*, 2019, **29**, 1806387.
80. G. K. Joshi, S. Deitz-McElyea, M. Johnson, S. Mali, M. Korc and R. Sardar, *Nano Lett.*, 2014, **14**, 6955-6963.
81. T. Liyanage, A. N. Masterson, H. H. Oyem, H. Kaimakliotis, H. Nguyen and R. Sardar, *Anal. Chem.*, 2019, **91**, 1894-1903.
82. A. J. Haes, S. Zou, G. C. Schatz and R. P. Van Duyne, *The Journal of Physical Chemistry B*, 2004, **108**, 6961-6968.
83. M. R. Zelio Fusco, Thanh Tran-Phu, Chiara Ricci, Alexander Kiy, Patrick Kluth, Enrico Della Gaspera, Nunzio Motta, Dragomir Neshev and Antonio Tricoli1, *Submitted* 2020.
84. H. Wang, D. W. Brandl, F. Le, P. Nordlander and N. J. Halas, *Nano Lett.*, 2006, **6**, 827-832.
85. P. V. Shinde, B. G. Ghule, N. M. Shinde, Q. X. Xia, S. Shaikh, A. V. Sarode, R. S. Mane and K. H. Kim, *New J. Chem.*, 2018, **42**, 12530-12538.
86. T. Witten Jr and L. M. Sander, *Phys. Rev. Lett.*, 1981, **47**, 1400.
87. J. J. Mock, R. T. Hill, Y.-J. Tsai, A. Chilkoti and D. R. Smith, *Nano Lett.*, 2012, **12**, 1757-1764.
88. S. S. Aćimović, H. Šípová, G. Emilsson, A. B. Dahlin, T. J. Antosiewicz and M. Käll, *Light: Science & Applications*, 2017, **6**, e17042-e17042.
89. https://www.engineeringtoolbox.com/refractive-index-d_1264.html, 2008.
90. X. Wang, H. Qin, J. Pei, Y. Chen, L. Li, J. Xie and J. Hu, *Journal of Rare Earths*, 2016, **34**, 704-710.
91. L. Gas, *Matheson gas products*, 2013, **22**.
92. A. Elfasakhany, *Engineering Science and Technology, an International Journal*, 2016, **19**, 1224-1232.
93. T. Tran-Phu, H. Chen, R. Bo, I. Di Bernardo, Z. Fusco, A. N. Simonov and A. Tricoli, *Energy Technology*, **0**, 1801052.
94. A. Karperien, *Charles Sturt University*, 2013.
95. A. Bard and L. Faulkner, *Electrochemical Methods: Fundamentals and Applications*, John Wiley & Sons, Inc, 2001.
96. A. B. Dahlin, J. O. Tegenfeldt and F. Höök, *Anal. Chem.*, 2006, **78**, 4416-4423.